APPLIED PHYSICS

Atomic-scale insights into the interfacial instability of superlubricity in hydrogenated amorphous carbon films

Xinchun Chen[1]*, Xuan Yin[1]*, Wei Qi[1], Chenhui Zhang[1†], Junho Choi[2], Sudong Wu[3], Rong Wang[1], Jianbin Luo[1†]

Copyright © 2020 The Authors, some rights reserved; exclusive licensee American Association for the Advancement of Science. No claim to original U.S. Government Works. Distributed under a Creative Commons Attribution NonCommercial License 4.0 (CC BY-NC).

The origin of instability or even disappearance of the superlubricity state in hydrogenated amorphous carbon (a-C:H) film in the presence of oxygen or water molecules is still controversial. Here, we address this puzzle regarding the tribochemical activities of sliding interfaces at the nanoscale. The results reveal that gaseous oxygen molecules disable the antifriction capacity of a-C:H by surface dehydrogenation of tribo-affected hydrocarbon bonds. In comparison, oxygen incorporation into the hydrocarbon matrix induces the formation of a low-density surface shear band, owing to which the friction state depends on the oxygen content. High friction of a-C:H film in humid environment originates from the "tumor-like" heterogeneous structures as formed in the highly oxidized tribolayer. Notably, an appropriate doping of silicon can completely shield the moisture effect by forming a silica-like tribolayer. These outcomes shed substantial lights upon the roadmap for achieving robust superlubricity of carbon films in a wide range of environments.

INTRODUCTION

Hydrogenated amorphous carbon (a-C:H) is a fantastic solid lubricant, which can nearly cancel out the interfacial friction forces between rubbing surfaces and decrease the friction coefficient μ to an extremely low level of a few thousandths (i.e., μ ~ 0.001) in macroscale (*1*–*4*). However, such a peculiar superlubricity phenomenon is generally encountered in dry inert gases (*3*–*7*), hydrogen atmosphere (*5*, *8*–*10*), or ultrahigh vacuum (*2*, *11*). It shows high sensitivity to oxygen-containing reactants such as water (*12*–*15*) and oxygen molecules (*12*, *15*–*17*) in the environment, and a trace amount of these species can completely disenable the antifriction performances of a-C:H films (*12*, *18*). Consequently, it is still a great challenge to achieve robust superlubricity in ambient atmosphere. To this end, extensive studies (*19*–*22*) have been implemented toward understanding the origin of environmental molecule–induced instability of superlow friction state in a-C:H films.

The key concern is the nature of surface and interface chemistry of a-C:Hs under the incursion of oxygen and water molecules (*13*, *15*, *21*, *23*, *24*). One possible explanation is the surface modification by gas adsorption (*14*, *20*, *21*, *25*). Previous work has found that, although the majority of gas molecules just physically adsorb on the a-C:Hs after exposure to ambient air, the hydrocarbon surfaces readily get oxidized when a small fraction of the adsorbed molecules undergo dissociation and form chemical bonds (*15*, *16*, *21*). A native oxide layer is therefore in situ formed, which is closely related to the high friction observed in the running-in stage (*21*, *26*). In addition, as compared to oxygen molecules, adsorbed water layers are expected to act as a stronger physical barrier due to its greater dipole interactions and the corresponding larger cohesive energy (*27*, *28*). Moreover, the presence of thicker water layers under high humidity can induce viscous drag and capillary forces between the sliding surfaces (*29*). Another crucial factor is the tribochemical reactions occurred along the sliding interface induced by these oxygen-containing adsorbates (*24*, *30*). Strong chemical interactions take place not only between the a-C:H film and the tribo-coupling materials but also between the contact surfaces and the gas species (*31*–*34*). During this process, tribo-induced structural transformation and material transfer are usually accompanied by the in situ formation of a newly constructed tribolayer in the contact area (*35*, *36*), which is a decisive aspect for the lubrication behaviors of a-C:H films. These achievements are quite meaningful for providing basic knowledge of gas-mediated frictional performances of a-C:Hs although the characterization methods such as Raman and x-ray photoelectron spectroscopy (XPS) used in these studies (*14*–*16*, *20*, *21*, *23*, *26*, *30*) cannot provide accurate quantification and visual inspection of the targeted area. Hence, the details of the most essential mechanisms governing the near-surface materials activities still remain vague, and several critical controversies need more in-depth clarification. To the best of our knowledge, there is no report yet about the experimental information of the buried sliding interface resolved at the levels of atomic-scale resolution, which are the key clues to clearly address these questions.

In light of these considerations, we used atomic-resolution spectra generated by scanning transmission electron microscopy (STEM) and electron energy-loss spectroscopy (EELS) to characterize the tribo-affected contact surfaces for the purpose of understanding how atoms are arranged along the buried interface and how the atomic-scale structure and elemental distribution affect the frictional properties of a-C:H films. The relevant details about the atomic-scale analysis procedures are described in our previous work (*35*). First, we design individual experiments to illuminate the oxygen effects on the hydrocarbon lubricating matrix from the extrinsic and intrinsic perspectives, respectively. Then, we explore the underlying fundamentals involved in the abnormal high friction in ambient air through the case study of a-C:H rubbing against bare steel. Last, we

[1]State Key Laboratory of Tribology, Department of Mechanical Engineering, Tsinghua University, Beijing 100084, China. [2]Department of Mechanical Engineering, The University of Tokyo, Tokyo 113-8656, Japan. [3]Academy for Advanced Interdisciplinary Studies, Southern University of Science and Technology, Shenzhen 518055, China.
*These authors contributed equally to this work.
†Corresponding author. Email: chzhang@tsinghua.edu.cn (C.Z.); luojb@tsinghua.edu.cn (J.L.)

present the methodology of which the humidity effect can be effectively shielded by tailoring the microstructure of a-C:H through foreign-element doping and stable superlubricity can be retained. The one-of-a-kind outcomes that we obtained have advanced the frontiers of scientific knowledge in a more unique manner in this work as compared to the earlier literatures, which implicitly mentioned or speculated on the origins of interfacial instability of superlubricity in amorphous carbon.

RESULTS

Microstructures and antifriction behaviors

The structures and properties of the as-grown hydrogen-rich a-C:Hs films are indicated in Fig. 1 (A to F). All the films were designed to have a bilayer structure (Fig. 1B), in which a hard silicon-containing a-C:H (a-C:H:Si) interlayer with a thickness of approximately 250 nm and strong adhesion to the substrates (Fig. 1, C and D) was first deposited before the subsequent growth of the targeted a-C:Hs layer. The total thickness of the film was controlled at about 1.0 μm. The pure a-C:H film (ACF-1) has a high content of hydrogen [39.3 atomic % (at %)] and maintain a reasonable hardness of 13.4 GPa. Two kinds of oxygen-doped a-C:H:O (oxygen-containing a-C:H) films with oxygen contents of 5.4 at % (ACFO-1, Fig. 1, E and F) and 9.5 at % (ACFO-2), respectively, were synthesized by introducing oxygen into the hydrocarbon matrix during deposition. The incorporation of oxygen slightly reduces the hydrogen content and the hardness of the films. Five types of silicon-doped a-C:H:Si films (ACF-2 to ACF-6) with gradually increased Si content from 4.2 to 9.3 at % were deposited to investigate the humidity shielding effect of silicon. All the films are in amorphous state (Fig. 1E) and have ultrasmooth surfaces with a Ra roughness of 0.1 to 0.2 nm.

The structural and atmospheric dependences of antifriction behaviors for these a-C:Hs films are demonstrated in Fig. 1 (G and H). In accordance with the previous work (*35*), a stable superlow friction coefficient of 0.008 (accompanied by an unmeasurable wear loss, Fig. 2A and fig. S1A) was readily achieved in dry N_2 for the self-mated pure a-C:H film (ACF-1, Fig. 1G). In comparison, the friction coefficient gradually increased from the initial value of 0.02 to a high level of 0.1 at the end of the test in dry O_2 atmosphere, which also induced noticeable material wear to the film surface (wear track depth of 23 nm, fig. S1B). Moreover, when comparing the Raman spectra (ACF-1, N_2 versus O_2) in Fig. 2B, the smaller photoluminescence (PL) background slope (usually proportional to the hydrogen content in the film) (*37*) indicates deeper surface structure modification of the a-C:H film after tested in O_2. The presence of environmental oxygen molecules would disenable the antifriction capacity of a-C:H film and was inferred to markedly change the interfacial contact states. Beyond our expectation is that, however, a small amount of oxygen incorporated into the hydrocarbon matrix could further lower the friction coefficient to an extremely level of 0.004 in dry N_2 (5.4 at % O, ACFO-1; Fig. 1G), although more tiny fluctuations occurred in the recorded friction coefficient curve and also nanoscale wear was caused on the film surface (wear track depth of 2 nm, fig. S1C). Nevertheless, further increase in the oxygen content to 9.5 at % (ACFO-2, Fig. 1G) caused stronger fluctuations in the friction curve, and the friction coefficient came up to 0.016 after undergoing a superlubricity state (2100 sliding cycles). Even so, the surface wear volume for ACFO-2 in N_2 (wear track depth of 7 nm, fig. S1D) is still much smaller than that of ACF-1 in O_2 atmosphere. However, the most notable finding is that the colors of the ball scar surfaces turned blue (ACFO-1, dry N_2; Fig. 2A) and light green (ACFO-2, dry N_2, Fig. 2A), respectively, for these two oxygen-doped films, implying structural changes after the friction test. This speculation is evidenced by the decreased PL background slope and shrinking of the *D*-peak in the Raman spectra (ACFO-1 versus ACFO-2, N_2, Fig. 2B) measured from the contact areas. In particular, for the ball scar surfaces, the PL backgrounds are almost leveled and the *D*-peaks (arising from the breathing vibrations of sp^2 sixfold aromatic rings) are nearly absent, suggesting substantial structural transformation of the hydrocarbon matrix.

In humid air (45% relative humidity, Fig. 1H), however, the friction behaviors of a-C:Hs films were significantly different from the cases in dry gaseous environments. For pure a-C:H film (ACF-1), the lubricity was largely deteriorated and the friction coefficient gradually increased from about 0.15 to 0.45, which caused severe wear to the contact surfaces [ACF-1, relative humidity (RH) 45%, Fig. 2A] with a wear track depth of 150 nm (fig. S1E). Meanwhile, the ball scar surface was covered by a brown tribolayer, indicating the formation of new structure phases during sliding. This speculation was supported by the Raman spectrum (ACF-1, air, Fig. 2B), in which the splitting of *D*- and *G*-peaks and the enhanced local clustering of sp^2 phases were observed. In comparison, incorporation of silicon into the hydrocarbon matrix emerges as an effective method to combat the high friction of a-C:H film. As shown in Fig. 1H, a quite small amount of Si (4.2 at %) could lower the friction coefficient to about 0.13 and further increase of Si content reduced the friction gradually. Specifically, a stable superlow friction coefficient of 0.006 was achieved for the a-C:H:Si film with a Si content of 9.3 at % (ACF-6). After the friction test, a dark brown wear scar was produced on the steel ball surface (ACF-6, RH45%, Fig. 2A). In addition, some wear debris was piling up surrounding the ball scar. Simultaneously, a mild wear track with a maximum depth of 40 nm (fig. S1F) was generated on the ACF-6 film surface. The loss of film material was speculated to be the source of the as-formed tribolayer and wear debris on the ball scar. Moreover, the Raman spectra (ACF-6, air, Fig. 2B) indicate that the wear track almost maintained its original film structure, while the wear scar and wear debris underwent phase transformation and became rich in newly formed sp^2-C phases.

Oxygen-induced softening of hydrocarbon sliding interface

To further clarify the underlying mechanisms behind these friction phenomena, we used state-of-the-art surface and interface analytical techniques such as time-of-flight secondary ion mass spectroscopy (TOF-SIMS), STEM and EELS. In particular, for the atomic-scale resolution imaging capability STEM, the fundamental principles and the preparation procedure of nanometer-thick lamella from the sliding surfaces using the focused-ion beam (FIB) lift-out method were described in the previous work (*35*). A key step is that a metallic Cr layer was first deposited to the contact surfaces for protection during ion thinning. The FIB slicing positions for the selected tribo-couples are indicated in Fig. 2A. Figures 3 and 4 compare the oxygen-induced structural evolutions of the a-C:Hs sliding interface from the extrinsic and intrinsic perspectives, respectively. It should be first pointed out that the bilayer structure was maintained for all the self-mated a-C:Hs tribo-couples after the friction tests, indicating that the rubbing actions occurred in the upper targeted layers. For pure a-C:H tested in O_2 atmosphere (extrinsic oxygen effect), there was no obvious structural change along the sliding interface of the ball wear scar as compared to the underlying bulk film (see cross-sectional

A

Code	Grown films*	Composition (at. %)					Hardness (GPa)	Elastic modulus (GPa)	Thickness (μm)	Roughness (nm)
		H	C	Si	O	N				
ACF-1	a-C:H layer	39.3	59.4	0.2	0.1	1.0	13.4	112.5	1.04	0.10
ACFO-1	a-C:H:O layer	37.4	56.6	0.0	5.4	0.6	11.8	91.9	0.95	0.12
ACFO-2	a-C:H:O layer	35.4	54.7	0.1	9.5	0.3	9.8	86.6	0.99	0.15
ACF-2	a-C:H:Si layer	43.5	50.6	4.2	1.1	0.6	11.5	93.6	0.93	0.17
ACF-3	a-C:H:Si layer	30.0	63.7	4.9	1.4	0.0	15.6	144.9	1.03	0.09
ACF-4	a-C:H:Si layer	35.3	56.3	5.7	1.5	1.2	14.0	123.8	1.11	0.14
ACF-5	a-C:H:Si layer	31.1	59.7	8.5	0.2	0.6	16.5	154.0	0.98	0.16
ACF-6	a-C:H:Si layer	31.9	57.2	9.3	1.2	0.4	16.2	155.7	1.01	0.13

*For all the grown films, a hard a-C:H:Si interlayer was first deposited on the substrates to serve as a bonding layer.

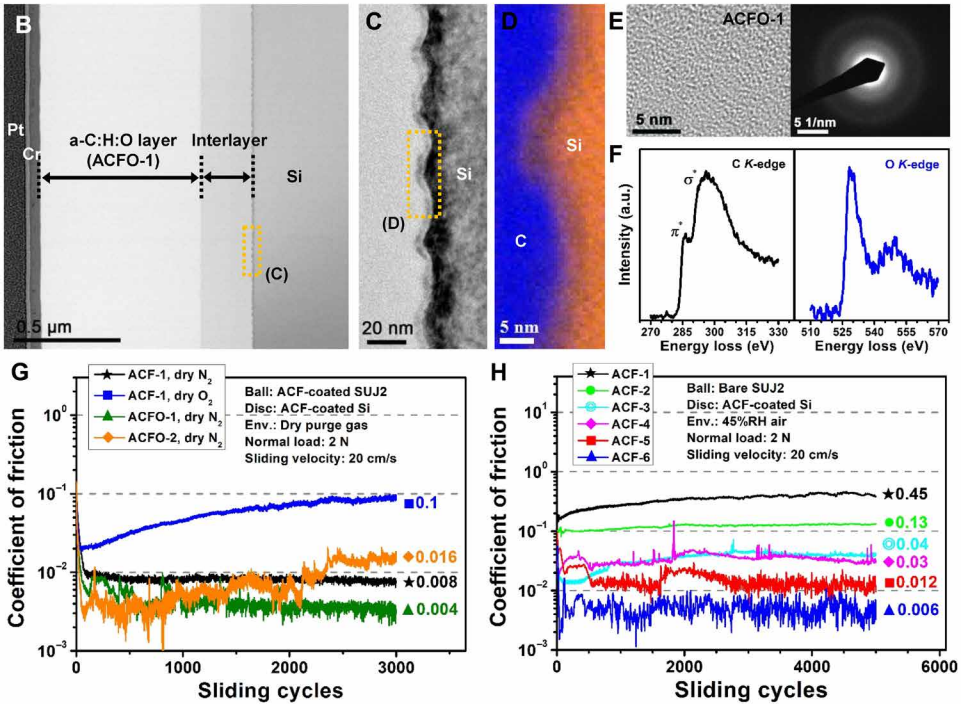

Fig. 1. Structures, compositions, mechanical properties, and frictional performances of a-C:Hs films. (**A**) Atomic composition and basic properties of the as-synthesized various kinds of a-C:Hs films. (**B**) The low-magnification cross-sectional bright-field (BF)–STEM image shows a typical bilayer structure of the a-C:H:O (designated as ACFO-1) film grown on Si wafer. (**C**) The high-magnification BF-STEM image and (**D**) the EELS spectrum image (SI) mapping image reveal that the high-energy ion implantation induced zig-zag interfacial morphology, confirming the excellent bonding adhesion of the interlayer to the Si wafer. (**E**) High-resolution TEM (HRTEM) image and diffraction pattern demonstrating the amorphous characteristic of the ACFO-1 film. (**F**) Measured C-*K* and O-*K* EELS spectra of the ACFO-1 film. a.u., arbitrary units. (**G**) Frictional behaviors of self-mated ACF-1, ACFO-1, and ACFO-2 tribo-couples in dry gaseous atmospheres of O_2 and N_2, for the purpose of evaluating the oxygen effect. (**H**) Frictional behaviors of a-C:H (ACF-1) and Si-doped a-C:H:Si (ACF-2 to ACF-6) films sliding against bare steel in ambient air, for the purpose of evaluating the humid effect.

TEM images in Fig. 3B). Similar interfacial morphology was also observed for the reference case of conducting in dry inert N_2 atmosphere (Fig. 3A). However, the TOF-SIMS depth-profiling results (Fig. 3C) clearly show that depletion of hydrogen from hydrocarbon groups such as H, CH, and C_2H was confirmed in the topmost 2-nm-thick region of the ball wear scar surface (relatively low TOF-SIMS intensity as compared to the bulk). Correspondingly, the amounts of oxygen-related species such as O and OH in this region are higher than that of the bulk. The presence of this oxygen-invaded sublayer was further confirmed by the three-dimensional (3D) TOF-SIMS image taken inside the ball wear scar (Fig. 3D), in which an oxygen-rich (carbon-deficient) near-surface layer was clearly observed. More vividly shown by the 2D TOF-SIMS image (Fig. 3E), the contact surfaces including the disc wear track and ball wear scar are rich in O and OH fragments while having much lower concentrations for hydrocarbon fragments (i.e., H, CH, and C_2H). However, it should be emphasized here that the above findings still cannot determine the exact assignments of the oxygen-related features of the C and O since TOF-SIMS is a characterization technique providing information about elemental composition rather than chemical bonding state. On the basis of the previous work by XPS (*38*, *39*), in the oxidizing environment, oxygen molecules can bond to carbon in

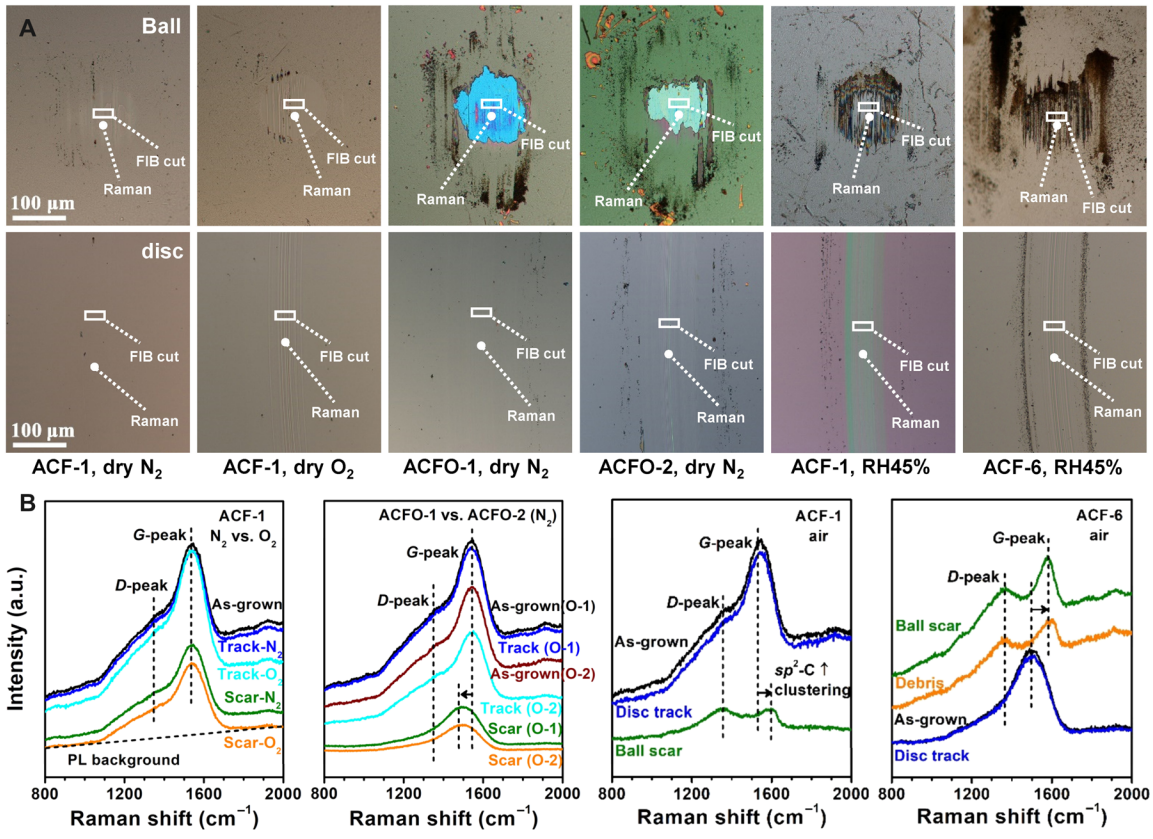

Fig. 2. Surface morphologies and Raman spectra of the a-C:Hs contact areas after the friction tests in Fig. 1 (G and H). (**A**) Optical images showing the ball wear scars and disc wear tracks for a-C:Hs in different environments. The FIB-slicing cites for preparing nanoscale-thick TEM lamellas and Raman measuring positions are also indicated in the images. (**B**) Raman spectra showing the structural evolutions of different contact surfaces by evaluating the changes of photoluminescence (PL) background, as well as the position and shape of *D*- and *G*-peaks.

several distinct ways, namely, the hydroxyl type of C—O—H, the ether type of C—O—C, and the ketone-type of C═O. These functional species are the most dominating groups involving oxygen on carbon film surface, which significantly affect the frictional behaviors of a-C:H film. The other less abundant groups containing oxygen are the peroxy radical, peroxy, and ketal (*40*). Since the —OH (low density in the present case due to the absence of water molecules in dry O_2) and C═O groups usually have the passivation effect (beneficial for friction reduction), the gradually increased friction observed in dry O_2 was speculated to be correlated with the plentiful formation of C—O—C bonds between the two sliding surfaces, which yielded a cold welding phenomenon and hence high adhesive forces.

In comparison, for oxygen-doped a-C:H:O films tested in dry N_2 atmosphere (intrinsic oxygen effect), the presence of oxygen in the hydrocarbon matrix induces much more different structural transformations along the sliding interface. The first interesting finding is that, although the ball wear scar surface became colorful after the friction test, the surface roughness was still maintained in an extremely low level. The Ra values of the two samples are 2.47 nm (Fig. 4A) and 4.37 nm (Fig. 4B), respectively, for oxygen contents of 5.4 and 9.5 at %. It seems that the relatively rough contact surface for higher oxygen content was also consistent with the observed higher friction coefficient (ACFO-2, Fig. 1G). More notable finding is that a shallow sublayer with low contrast in high-resolution TEM (HRTEM) image is found in the topmost region along the sliding interface, of which the thickness increases from 5 nm (Fig. 4C) to 10 nm (Fig. 4D) when the oxygen content increasing from 5.4 to 9.5 at %. However, such a shallow band is not observed in the corresponding disc wear track (Fig. 4E). In general, brighter contrast in HRTEM image stands for lighter element and lower density in the observed microstructure. This speculation can be further confirmed by STEM characterization (Fig. 4, F to H). As clearly shown by the bright-field (BF)–STEM image in Fig. 4F, this shallow shear band seems to be loosened as compared to the underlying pristine a-C:H:O (ACFO-2) bulk, and its microstructure is still in an amorphous state. The EELS spectrum image (SI) elemental maps in Fig. 4G further illuminate that this shear band is mainly composed of carbon (C-*K* map) and the oxygen concentration (O-*K* map) is significantly reduced as compared to the bulk region. However, oxygen is locally enriched in the transition region between the shallow band and the bulk. These findings explicitly demonstrate that the presence of oxygen in the hydrocarbon matrix could induce redistribution of interfacial atoms during rubbing and hence the reconstructing of the sliding interface. To quantitatively clarify the bonding structure of the tribo-area, EELS core edge spectra were recorded point by point across this shallow shear band, as shown in Fig. 4H. The major characteristic of the measured C-*K* edges is the gradually decreased sharpening of π* peaks at 285.5 eV (*41*) from the near surface area (curve 1) across the shear band (curves 2 to 5) to the bulk (curves 6 and 7). Correspondingly, oxygen (O-*K* edges) is mainly involved in

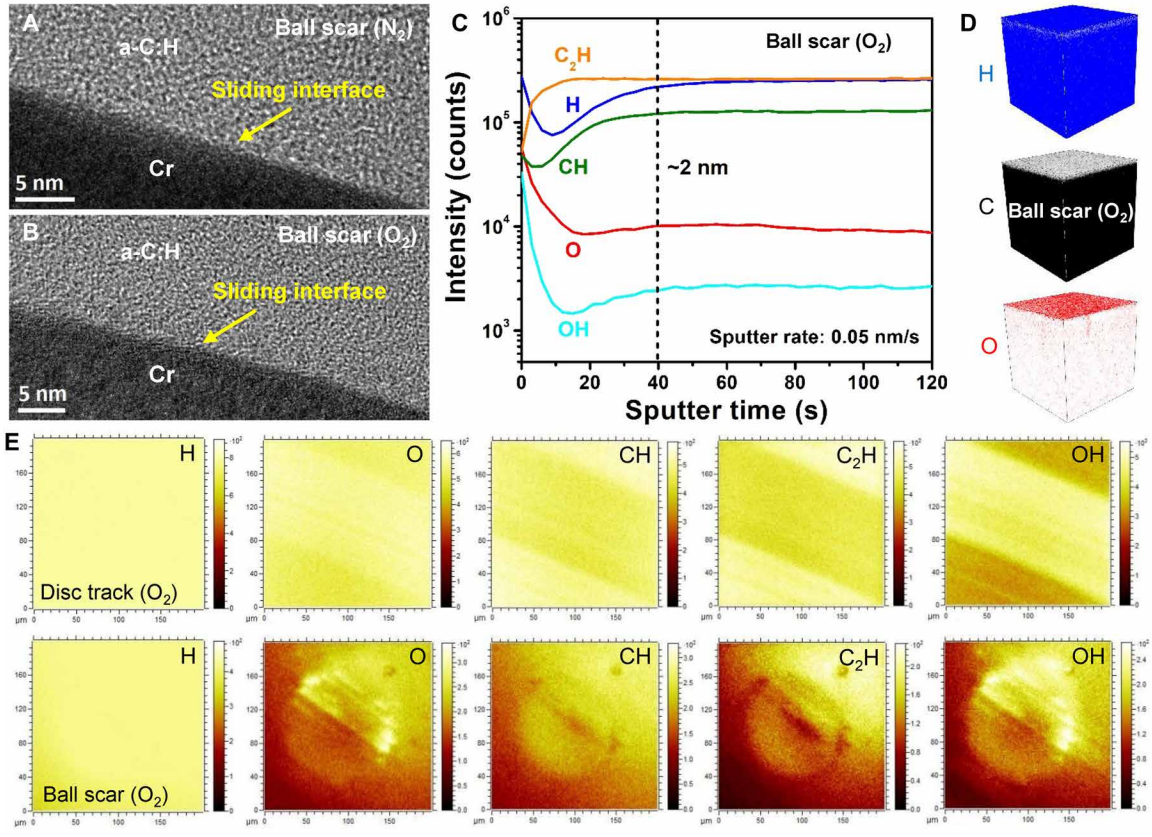

Fig. 3. Interfacial microstructures and surface chemistry of self-mated a-C:H films after the friction tests in dry N_2 and O_2 gaseous atmospheres (ACF-1, Fig. 1G). (**A** and **B**) HRTEM images showing the microstructures of the a-C:H sliding interfaces from the ball wear scars resulted from dry N_2 and O_2, respectively. (**C**) TOF-SIMS intensity spectrum revealing the chemical composition of the ball wear scar as a function of profiling depth. A tribo-affected sublayer with a thickness of 2 nm was detected. (**D**) 3D TOF-SIMS image further confirming the existence of an oxygen-rich (carbon-deficient) near-surface layer. (**E**) 2D TOF-SIMS images showing the distributions of chemical fragments within the disc wear track and ball wear scar.

the formation of π*(C═O) (at 532.5 eV) or σ*(C—O) (at 542 eV) bonds (*42*). The bonding density is locally high in the transition region (curves 4 and 5), which is consistent with the above SI mapping result. The calculated carbon bonding fractions (Fig. 4I) based on the C-*K* edges (*43*) further indicate that this shear band had a high density of sp^2(C═C) phase as compared to sp^3-bonded phases, for which the fraction gradually decreased from 66% in the outermost region (point 1) to 37% in the transition region (point 5), in comparison to that of the bulk (30%, points 6 and 7). In consideration of the nearly vanishing *D*-peak in the Raman spectrum (ball scar of ACFO-2, N_2, Fig. 2B), it is reasonable to speculate that the sp^2 phase is mainly in the form of chain-like structure. For the oxygen-related carbon bonds (*44*), the bonding density of π*(C═O) bonds was in a low level (about 5%) for this shear band except the position near the transition region (13%, point 4). In addition, the σ*(C—O) bond was in the overlapped position with σ*(C—H) bond, and therefore, the exact bonding fraction of each bond could not be completely determined (*45*). As a whole, the sum of fractions of sp^3(C—H) and sp^3(C—O) increased from 27.5 to 45% across this shallow sublayer from the sliding surface to the bulk of the film. For the low oxygen content of 5.4 at %, the as-formed ketone-type functional group of C═O was beneficial for reducing the friction owing to their passivation effect. However, for a higher oxygen content of 9.5 at %, the formation of ether-type bonding features of C—O within the shear band increased the probability of adhesive interactions between the two sliding surfaces, which resulted in the stronger fluctuations in the friction curve and the increase of friction coefficient from 0.004 to 0.016 (ACFO-2, Fig. 1G). The residual fraction was assigned to the σ* bonding of sp^3(C—C). In addition, the mass density of this tribo-affected sublayer, calculated by the plasmon energy in the low-loss spectrum (fig. S2), was about 1.5 to 1.75 g/cm^3 (cf. 2.27 g/cm^3 of graphite), confirming the tribo-induced softening (low density) characteristic of the hydrocarbon sliding interface.

Humidity-induced tribochemical eroding of carbonaceous surfaces

As observed above, the abnormal high friction of a-C:H films in humid ambient environments was highly correlated with the humidity-induced material transfer and interactions in the contact areas. As clarified by the BF-STEM image in Fig. 5A, the as-formed tribolayer on the ball wear scar surface is very thick (thickness of ~250 nm), implying that continuous tribochemical reactions occurred and new phases formed during the sliding process. As more clearly shown by high-angle annular dark-field (HAADF)–STEM image in Fig. 5B, the tribolayer is found to be composed of several sublayers including a "tumor-like" nanocluster-distributed amorphous sublayer near the sliding surface (Fig. 5C), an iron oxide nano-crystallites/amorphous domains–mixed interlayer in the middle (Fig. 5D), and an iron-based

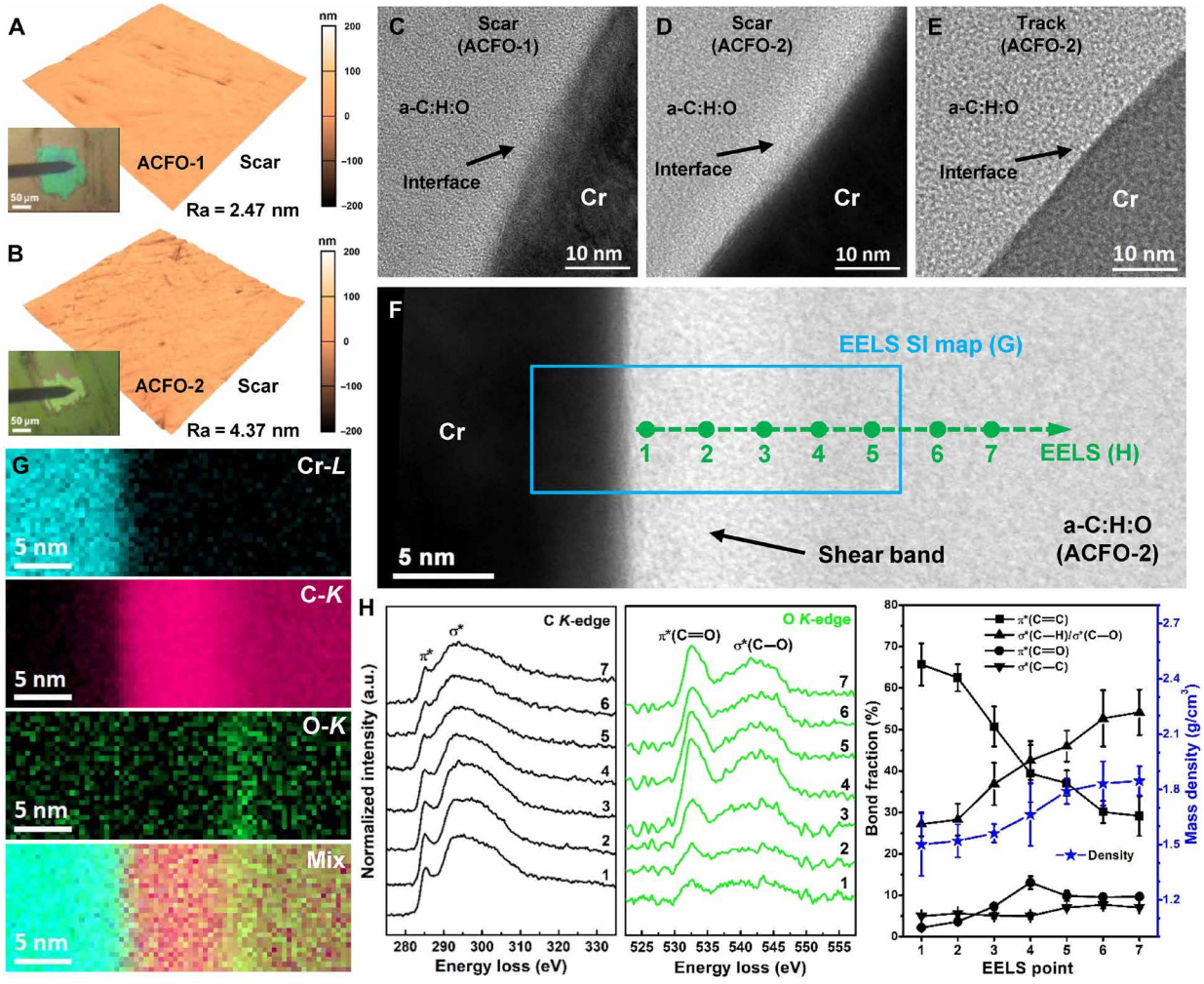

Fig. 4. Surface morphologies and interfacial microstructures of self-mated a-C:H:O films after the friction tests in dry N_2 gaseous atmosphere (ACFO-1 and ACFO-2, Fig. 1G). (**A** and **B**) 3D atomic force microscopy images showing the ultrasmooth wear scar surfaces of ACFO-1 and ACFO-2, respectively. The insets are the optical images captured during probe scanning. (**C** to **E**) HRTEM images showing the bonding structures from different sliding interfaces: (C) ball wear scar for ACFO-1, (D) ball wear scar for ACFO-2, and (E) disc wear track for ACFO-2. (**F**) BF-STEM image showing the existence of a shallow shear band on top of the bulk a-C:H:O (ACFO-2). The positions for EELS SI mapping and line acquisition are also indicated. (**G**) EELS Cr-*L*, C-*K*, and O-*K* maps and their composite showing the elemental distribution along the sliding interface as marked in (F). (**H**) Evolution of EELS C-*K* and O-*K* core edge spectra recorded across the shear band as marked in (F). (**I**) Carbon bonding fractions calculated from the C-*K* core edges in (H) and the mass density estimated from the plasmon energy in the low-loss spectra (fig. S2).

highly oxidized and crystallized bottom layer near the steel ball surface (Fig. 5E). The increasing crystallization across the tribolayer is clearly confirmed by the fast Fourier transform insets, in which a diffused ring (Fig. 5C) gradually evolves into diffraction pattern with a series of spots (Fig. 5E). Meanwhile, according to the elemental contrast in HAADF-STEM (Fig. 5B) or BF-STEM (Fig. 5, C to E) images, the mass density also seems to gradually increase from the near-surface sublayer through the interlayer then to the bottom layer. This observation and the relevant bonding states of the tribolayer are further analyzed by EELS. As shown in Fig. 5F, the EELS SI elemental maps of C-*K*, O-*K*, and Fe-*L* indicate that carbon, oxygen, and iron are distributed throughout the tribolayer. In particular, the tumor-like nanoclusters are mainly composed of carbon, and the oxygen and iron contents are relatively low as compared to the interlayer and the bottom layer. Also note that the interface between the tribolayer and the steel surface is quite straight, and it seems that the contact surface had been tribochemically eroded during sliding. Along with the shearing process, iron atoms could then diffuse into the tribolayer and form new phases throughout the entirety of the tribolayer. The elemental profile (Fig. 5G) across the tribolayer measured by EDS (energy-dispersive x-ray spectroscopy) quantitatively confirms the multiple layer structure observed above. Combined with the plasmon energies E_p (Fig. 5G) from the low-loss spectra, the mass densities of the tumor-like nanoclusters (points 1 to 4) were calculated to be in the range of 2 to 2.5 g/cm^3, and then it gradually increased across the tribolayer (points 5 to 10), and lastly to 7.4 g/cm^3 for the steel bulk (point 11). Figure 5H shows EELS SI line profiles of C-*K*, O-*K*, and Fe-*L* core edges acquired point by point across the tribolayer, and the evolution of bonding states for each element is explicitly clarified. As seen, carbon signal is extensive in the nanocluster-distributed amorphous sublayer, and it is mainly involved in forming sp^2-C phases in this region and its vicinity, as revealed by the obviously emerging π^* peaks in the C-*K* core edges (EELS C-*K* curves 1 to 5). The O-*K* and Fe-*L* core edges once again verify the distribution of

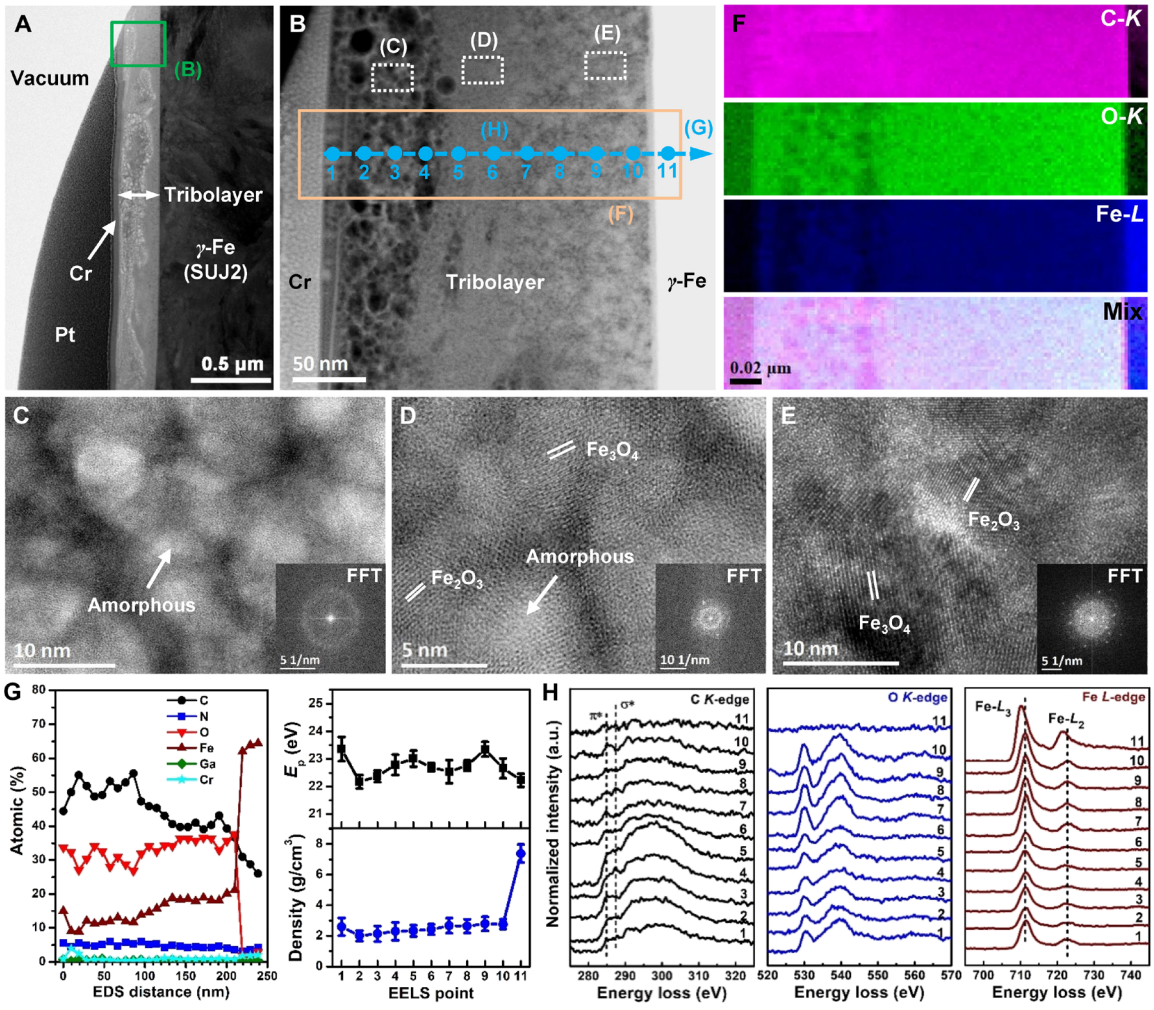

Fig. 5. Microstructures of the tribolayer formed on bare steel ball surface after sliding against a-C:H film in humid air (ACF-1, Fig. 1H). (**A**) Low-magnification BF-STEM image showing a tribolayer with a thickness of 250 nm formed on bare steel ball surface. (**B**) HAADF-STEM image indicating the tribolayer is mainly composed of three sublayers, marked as (C), (D), and (E). (**C** to **E**) High-magnification BF-STEM images clarifying the microstructures of the as-observed three sublayers in (B): a tumor-like nanocluster-distributed amorphous sublayer near the sliding surface (C), an iron oxide nano-crystallites/amorphous domains mixed interlayer in the middle (D) and an iron-based highly oxidized and crystallized bottom layer near the steel ball surface (E). Insets are the corresponding fast Fourier transform (FFT) images for each sublayer. (**F**) EELS SI maps of C-*K*, O-*K*, Fe-*L*, and their composite image show the elemental distribution across the tribolayer, as marked in (B). (**G**) EDS elemental distribution across the tribolayer as marked in (B). The simultaneously recorded plasmon energies and the calculated mass densities are also indicated. (**H**) Evolution of EELS C-*K*, O-*K*, and Fe-*L* core edges acquired point by point across the tribolayer as marked in (B).

these two elements throughout the entire tribolayer, whereas they were specifically enriched in the highly oxidized bottom layer (EELS curves 7 to 10). On the counterface disc side, besides the significant material loss (wear track depth of 150 nm, fig. S1E), the a-C:H film surface was also highly oxidized with a tribo-affected depth of 10 nm (STEM images and EELS O-*K* curves, fig. S3). This is in contrast to the nearly intact a-C:H film after the superlubricity test in dry N_2. Apparently, the abnormal high friction in humid air is the result of growth of such a highly oxidized and covalently bonded tribolayer, especially the formation of an adhesive tumor-like topmost working layer along the sliding interface.

Si-triggered interfacial nanostructure to shield moisture effect

In contrast to the high friction of a-C:H in humid air, silicon incorporation has significantly modified the interfacial structures and retained the superlubricity states for a-C:H:Si. As indicated by the low-magnification HAADF-STEM image in Fig. 6A, the bare steel ball is likely to maintain its pristine surface without noticeable wear loss (i.e., original winding interface, as compared to the tribochemically polished straight interface for a-C:H in Fig. 5A) after the friction test. A more interesting finding from the inset high-magnification BF-STEM image is that the contact surface is actually covered by an in situ formed nanoscale tribolayer with a thickness of ~5 nm. The enlargement shown by the BF-STEM image in Fig. 6B further clarifies that the tribolayer is mainly amorphous and well bonded to the steel surface. Moreover, almost no obvious iron-related nanoparticles (as those observed in Fig. 5 for a-C:H film) are found in the tribolayer, confirming the near-wearless behavior of the steel ball surface and the corresponding protection effect from the tribolayer. The composition and elemental distribution of this tribolayer were more delicately analyzed by HAADF-STEM and EDS mapping.

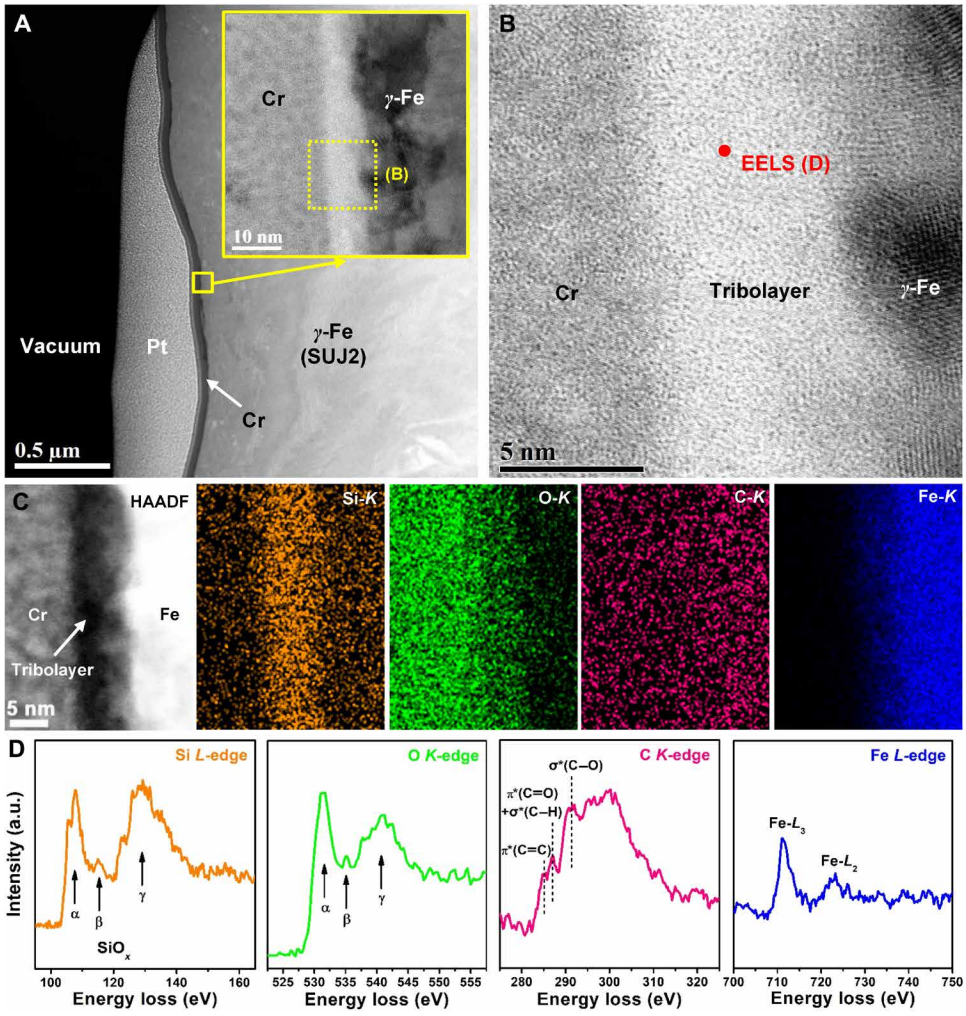

Fig. 6. Microstructures of the antimoisture tribolayer formed on bare steel ball surface after sliding against a-C:H:Si film in humid air (ACF-6, Fig. 1H). (**A**) Low-magnification HAADF-STEM image showing the retained winding interface of the bare steel ball surface after the superlubricity test. The inset BF-STEM image indicates the existence of a nanoscale tribolayer with a thickness of 5 nm formed on the contact surface. (**B**) High-magnification BF-STEM image showing the tribolayer is mainly amorphous and well bonded to the steel surface as marked in (A). (**C**) HAADF-STEM image and the corresponding EDS maps showing the elemental distributions of Si-*K*, O-*K*, C-*K*, and Fe-*K* within the tribolayer. (**D**) The EELS Si-*L*, O-*K*, C-*K*, and Fe-*L* core edges acquired from the central position of the tribolayer as marked in (B).

As shown in Fig. 6C, the tribolayer was detected to be mainly composed of silicon and oxygen because of the overwhelming intensities in Si-*K* and O-*K* maps. Therefore, it is reasonable to speculate that the main body of this tribolayer is based on silicon oxide. Nevertheless, it should be pointed out that the above tribolayer was lifted out by FIB from the central region of the wear scar in consideration of the fact that this area was, most of the time, in contact during sliding. It was speculated to be playing the most substantial role in establishing and maintaining a superlubricity state. From the scar center to the scar edge, however, the thickness of the tribolayer gradually increased from 5 nm through 18.5 to 165 nm, as revealed in fig. S4. This might be caused by the film material transfer from the contact center to the border along the sliding direction, which resulted in the continuous growth and thickening of the tribolayer formed in the position away from the central region. Thus, the nanostructured tribolayer formed in the core contact area is competent to achieve a stable superlubricity state even it is only a few nanometers thick. In addition, as revealed by the HAADF-STEM image and Fe-*K* map, the shallow band between the tribolayer and the steel surface once more emphasizes the excellent bonding strength between them through chemical alloying. The EELS Si-*L*, O-*K*, C-*K*, and Fe-*L* core edge spectra measured in the central position (as marked in Fig. 6B) provide more accurate structural information of the tribolayer. As shown in Fig. 6D, three characteristic peaks (α, β, and γ) due to different electron excitation states (*46*) are distinguished in the Si-*L* and O-*K* core edges, which clearly verify that the main bonding state of this nanostructured tribolayer is a silica-like tetrahedrally coordinated silicon compound. Meanwhile, a certain amount of carbon and trace of iron are confirmed in the C-*K* and Fe-*L* core edges. Correspondingly, a thin silica-like oxidized layer (~5 nm) was also detected on the rubbing a-C:H:Si film surface (fig. S5). Thus, it is quite valid to argue that this in situ formed hydrophilic tribolayer is capable of shielding the moisture effect or even taking advantage of the water molecules to realize superlow friction.

DISCUSSION AND CONCLUSIONS

The above achievements clearly indicate that the stability of a superlubricity state in a-C:H is highly correlated with the environmental gaseous characteristics. Depending on the tribochemical interactions between the carbon surfaces and gaseous species, the contact area usually undergoes redistribution of interfacial atoms and the reconstruction of the outermost surface layer as well as the in situ formation of interfacial nanostructures, which consequently affect the friction forces arising at the sliding interface.

Specifically, it is capable for self-mated a-C:H surfaces to maintain the hydrogen passivation–induced superlubricity state in dry inert gas such as N_2 without detectable surface wear loss under the contact pressure of 0.68 GPa (ACF-1, dry N_2, Figs. 1G and 2A). This superlow friction state is extremely stable in dry N_2 even under a high contact pressure of up to 1.17 GPa despite that nanoscale wear loss occurred to the hydrocarbon surface (*35*). The occurrence of nanoscale wear was accompanied by local clustering and ordering of sp^2-C phase in the outermost ~3-nm region, which favored the further reduction of friction coefficient. Nevertheless, in O_2 atmosphere, the sustained oxygen invading toward the contact area causes the depletion of hydrogen atoms from the hydrocarbon bonds such as H, CH, and C_2H in the topmost 2-nm-thick region of a-C:H film (Fig. 3C), yielding an oxygen-rich near-surface sublayer. However, the extrinsic oxygen molecules were only capable of inducing structural perturbations in this shallow region, and the bonding structure of the underlying bulk film remained intact as revealed by the Raman spectra and TOF-SIMS results (ACF-1, dry O_2, Fig. 2B and Fig. 3, B to D). The DFT calculations (*47*, *48*) imply that chemisorption of O_2 molecules on C—C bonds of hydrocarbon chains can trigger the breaking of C—C bonds and lastly cause the cleavage of the chains. A CO-terminated subchain is then produced on hydrocarbon surfaces. Further adsorption of oxygen molecules on this active site shortens the chain length through the formation and release of CO_2. Therefore, the oxygen etching of the hydrocarbon network and the formation of adhesive phases should significantly contribute to the increased friction and noticeable wear of a-C:H surfaces (ACF-1, dry O_2, Figs. 1G and 2A and fig. S1B). In comparison, the incorporation of oxygen into the hydrocarbon matrix not only modifies the film structure but also endows the sliding interface with a new antifriction mechanism. Upon contact, the presence of oxygen triggers the redistribution of interfacial atoms and promotes the formation of a low-density shear band. For a relatively low content of oxygen (5.4 at %, ACFO-1), the softening of the sliding interface to an appropriate extent and the presence of a 5-nm-thick shear band is beneficial for further lowering the friction coefficient to 0.004 (c.f. 0.008 for pure ACF-1). However, more oxygen incorporation (9.5 at %) broadens this shear band, and the sliding interface is becoming more adhesive because of the development of a chain-like sp^2-rich bonding structure, which consequently results in the as-observed increase of friction coefficient (0.016 for ACFO-2, Fig. 1G). In view of this point, suitable oxygen doping is supposed to pave a new way for tailoring the physicochemical characteristic of the lubrication interface in amorphous carbon.

When rubbing against steel counterface, the major obstacle for a-C:H film to achieve low friction in humid air is the intensive tribochemical reactions occurring between the two contact surfaces (*49*–*51*). In the presence of water and oxygen molecules, the interfacial materials are continuously eroded, and large amounts of adhesive phases such as highly oxidized iron-based nanocrystallines and amorphous carbon domains (Fig. 5, B to E) are formed in the tribolayer during the sliding process. Besides the eroding of steel counterface, the subsurface of a-C:H film with a depth of 10 nm (EELS O-*K* curves, fig. S3C) is also highly oxidized. It seems that a lubricative layer cannot be formed along the sliding interface to effectively prevent the two rubbing surfaces from direct contact. Moreover, the formation of an adhesive tumor-like topmost working layer (Fig. 5C) further deteriorates the lubricity of the carbonaceous interface. In comparison, the doping of silicon into the carbon matrix provides a fantastic pathway to suppress the moisture effect from the ambient environment. Upon contact, a nanoscale silica-like tribolayer is immediately in situ formed on the steel surface through the material transfer from the a-C:H:Si film surface. The presence of this tribolayer is effective to protect the steel counterface from the moisture attack although its thickness is only 5 nm (Fig. 6B). It is speculated that the incorporation of Si into the a-C:H matrix is capable to lower the friction by using these gaseous species to form a hydrophilic silicon oxide surface and the relevant water-mediated aqueous lubrication (*52*, *53*). As also noticed by other researchers (*54*, *55*), the OH-rich surface on silicon oxide can induce the oriented growth of adsorbed water layers through hydrogen bonds with the surface OH groups and between water molecules. Under an appropriate relative humidity, a highly oriented (i.e., layer-like structure) network of water molecules can even be developed along the sliding interface (*56*), which provides an easy-shear pathway to lower the friction. It is worth emphasizing that the quality of adsorbed water layer (the corresponding friction reduction level) should be highly dependent on the surface density of OH groups, namely, the hydroxylation level of carbon surface controlled by the Si incorporation content. Theoretically, the molecular dynamics simulations on an OH-terminated silicon surface (*57*) also provides evidence for this argument that water molecules can still be arranged in a layered structure under high shear stress. The as-formed aqueous shear layer through water adsorption together with tribo-induced water dissociation can act as a boundary lubrication film (*58*, *59*) to reduce interfacial friction. Therefore, the in situ formation of a nanostructured tribolayer with well-organized hydroxyl groups in the running-in stage is a productive strategy to combat the moisture attack and to construct a stable superlubricious interface in amorphous carbon. The dissociative formation of a hydrophilic surface and the as-induced nanostructure of interfacial water molecules under sliding contact are the key opportunities for the occurrence of superlubricity. However, it should be pointed out here that besides the contribution of hydroxyl termination and adsorbed water layer to the lubricity, the role of surface atoms such as carbon and their arrangement patterns is also significant in achieving the superlubricity state. For instance, as revealed from large-scale quantum molecular dynamics simulations on water film–lubricated diamond surfaces, carbon atoms are involved in forming highly passivated surface chemical groups such as hydrogen-, hydroxyl-, keto-, and ether-terminated functional groups as well as aromatic Pandey carbon passivation asperities along the sliding interface (*60*). The friction reduction regime highly depends on the water surface density and the distribution fraction of each functional group. Consequently, the synergetic effects from different scenarios are responsible for the friction reduction or even vanishment in an a-C:H:Si tribo-system exposed to humid air.

In summary, at the atomic scale, we have successfully clarified the critical issue regarding the stability of sliding interface in superlubricious amorphous carbon subjected to various gaseous atmospheres. The results unequivocally highlight the decisive role of atomic

activities along the rubbing surface and the in situ formed tribolayer in the establishment of a robust antifriction interface. The friction-vanishing state is dependent on the tribo-induced interfacial nanostructures and their physicochemical interactions with the gaseous molecules. A feasible pathway is acknowledged to overcome the moisture-induced dilemma for a-C:H by forming a hydrophilic tribolayer and its synergetic corroborations with water molecules. The possibilities of realizing superlubricity states in intricate environments are promising for engineering these antifriction carbon lubricants in general. These findings can also be expanded as new theoretical knowledge edges for designing other unprecedented interfacial materials cherished with previously unidentified nanostructures and tailored properties.

MATERIALS AND METHODS

Synthesis of amorphous carbon films

Amorphous carbon films, including a-C:H, a-C:H:O, and a-C:H:Si, were synthesized by an ion vapor deposition system. The setup of this coater and the relevant details about deposition procedure have been reported elsewhere (*61*). The composition and structure of the films are tailored by introducing different gas sources such as toluene, toluene/oxygen mixture, and toluene/tetramethylsilane mixture. The basic properties of the as-synthesized films are summarized in Fig. 1 (A to F).

Superlubricity experiments

The friction experiments were conducted using an atmosphere-controlled ball-on-disc tribometer at room temperature. Different gaseous environments including dry N_2, dry O_2, and humid air (45 ± 1% RH) were established by purging distinct gaseous sources into the tribometer chamber. The ACF film–coated Si wafer was fixed on a rotary platform using a bare or film-coated SUJ2 bearing steel ball of 6 mm in diameter as a counterbody. The applied normal load was set at 2 N, yielding initial mean and peak Hertz contact pressures of 0.45 and 0.68 GPa, respectively. The choice of 2 N was mainly based on the fact that the contact pressure produced at a higher normal load such as 5 or 10 N was too high to establish a superlubricity state for a-C:H:Si film in humid air, since the occurrence of superlow friction in this case mainly originated from the formation of a hydrophilic silica gel–like tribolayer and the following aqueous shear layer. As for a smaller load such as 1 N, there would be a large number of vibrations or local instabilities in the recorded friction coefficient when the superlubricity state was achieved. During friction test, the rotary radius was set at 3.5 mm, and the linear sliding velocity was 20 cm/s. The total sliding distances for the dry (N_2 and O_2) and humid air cases were 65.9 and 109.9 m, respectively.

Characterizations

The morphologies of the contact surfaces were evaluated with a Nikon optical microscope. The topographies and cross sections of the wear tracks were measured by a laser-interference surface profilometer (Zygo NewView 8000). In some cases, the morphologies of the contact areas were recorded by atomic force microscopy (Asylum Research MFP 3D). The bonding information of the pristine films, the tribo-affected films, and the as-formed tribolayer was acquired using a Raman spectroscopy (Horiba JobinYvon HR800) with an Ar^+ laser wavelength of 514.5 nm. The surface chemistry states of the contact areas were assessed by a TOF-SIMS (ION-TOF GmbH). The nanoscale-thick lamellar specimens for TEM, STEM, and EELS observations were fabricated by a dual-beam scanning electron microscopy/FIB system (FEI Quanta 3D FEG) using an in situ lift-out technique. A field-emission HRTEM (JEOL 2010F) was used for a rough evaluation of the quality of the lamellar specimens. For STEM *z*-contrast imaging observation, the state-of-the-art dual aberration–corrected cold field-emission gun STEM (JEOL JEM-ARM200F) equipped with a Gatan GIF Quantum EELS spectrometer was used. The acceleration voltage was 200 kV, yielding a BF imaging resolution of 0.14 nm and a HAADF resolution of 0.08 nm. The details regarding the parameters and data acquirement can be found in the previous work (*35*). Also, the analysis methodology for the EELS SI mapping, plasmon energy, mass density, and bonding fraction calculations based on C-*K* core edges are referenced therein.

SUPPLEMENTARY MATERIALS

Supplementary material for this article is available at http://advances.sciencemag.org/cgi/content/full/6/13/eaay1272/DC1

Fig. S1. Surface morphologies and cross sections of the wear tracks produced on amorphous carbon film surfaces after the friction tests as shown in Fig. 1 (G and H).

Fig. S2. Evolution of EELS low-loss spectra recorded across the shallow shear band as marked in Fig. 4F and the derived E_p values through peak fitting.

Fig. S3. STEM and EELS characterization of the wear track formed on a-C:H film surface after sliding against bare SUJ2 steel ball in humid air (ACF-1, Fig. 1H).

Fig. S4. FIB slicing and TEM characterization confirming the variable thicknesses of the tribolayer in different contact positions of the wear scar formed on bare steel ball surface after sliding against a-C:H:Si film in humid air (ACF-6, Fig. 1H).

Fig. S5. STEM and EELS characterization of the wear track formed on a-C:H:Si film surface after sliding against bare SUJ2 steel ball in humid air (ACF-6, Fig. 1H).

REFERENCES AND NOTES

1. J. Robertson, Diamond-like amorphous carbon. *Mater. Sci. Eng. R* **37**, 129–281 (2002).
2. C. Donnet, J. Fontaine, A. Grill, T. Le Mogne, The role of hydrogen on the friction mechanism of diamond-like carbon films. *Tribol. Lett.* **9**, 137–142 (2000).
3. A. Erdemir, O. L. Eryilma, G. Fenske, Synthesis of diamondlike carbon films with superlow friction and wear properties. *J. Vac. Sci. Technol. A* **18**, 1987–1992 (2000).
4. D. Berman, S. A. Deshmukh, S. K. R. S. Sankaranarayanan, A. Erdemir, A. V. Sumant, Macroscale superlubricity enabled by graphene nanoscroll formation. *Science* **348**, 1118–1122 (2015).
5. X. Chen, T. Kato, M. Nosaka, Origin of superlubricity in a-C:H:Si films: A relation to film bonding structure and environmental molecular characteristic. *ACS Appl. Mater. Interfaces* **6**, 13389–13405 (2014).
6. P. Manimunda, A. Al-Azizi, S. H. Kim, R. R. Chromik, Shear-induced structural changes and origin of ultralow friction of hydrogenated diamond-like carbon (DLC) in dry environment. *ACS Appl. Mater. Interfaces* **9**, 16704–16714 (2017).
7. Y. Wang, K. Gao, B. Zhang, Q. Wang, J. Zhang, Structure effects of sp^2-rich carbon films under super-low friction contact. *Carbon* **137**, 49–56 (2018).
8. A. Erdemir, O. L. Eryilmaz, S. H. Kim, Effect of tribochemistry on lubricity of DLC films in hydrogen. *Surf. Coat. Technol.* **257**, 241–246 (2014).
9. H. Okubo, R. Tsuboi, S. Sasaki, Frictional properties of DLC films in low-pressure hydrogen conditions. *Wear* **340-341**, 2–8 (2015).
10. M. Nosaka, R. Kusaba, Y. Morisaki, M. Kawaguchi, T. Kato, Stability of friction fade-out at polymer-like carbon films slid by ZrO_2 pins under alcohol-vapored hydrogen gas environment. *Proc. Ins. Mech. Eng. Part J: J. Eng. Tribol.* **230**, 1389–1397 (2016).
11. X. Liu, J. Yang, J. Hao, J. Zheng, Q. Gong, W. Liu, A near-frictionless and extremely elastic hydrogenated amorphous carbon film with self-assembled dual nanostructure. *Adv. Mater.* **24**, 4614–4617 (2012).
12. C. Donnet, T. Le Mogne, L. Ponsonnet, M. Belin, A. Grill, V. Patel, C. Jahnes, The respective role of oxygen and water vapor on the tribology of hydrogenated diamond-like carbon coatings. *Tribol. Lett.* **4**, 259–265 (1998).
13. J. Sánchez-López, A. Erdemir, C. Donnet, T. Rojas, Friction-induced structural transformations of diamondlike carbon coatings under various atmospheres. *Surf. Coat. Technol.* **163-164**, 444–450 (2003).
14. H. Li, T. Xu, C. Wang, J. Chen, H. Zhou, H. Liu, Tribochemical effects on the friction and wear behaviors of a-C:H and a-C films in different environment. *Tribol. Int.* **40**, 132–138 (2007).

15. A. Alazizi, A. Draskovics, G. Ramirez, A. Erdemir, S. H. Kim, Tribochemistry of carbon films in oxygen and humid environments: Oxidative wear and galvanic corrosion. *Langmuir* **32**, 1996–2004 (2016).
16. K. D. Koshigan, F. Mangolini, J. B. McClimon, B. Vacher, S. Bec, R. W. Carpick, J. Fontaine, Understanding the hydrogen and oxygen gas pressure dependence of the tribological properties of silicon oxide–doped hydrogenated amorphous carbon coatings. *Carbon* **93**, 851–860 (2015).
17. L. Wang, L. Cui, Z. Lu, H. Zhou, Understanding the unusual friction behavior of hydrogen-free diamond-like carbon films in oxygen atmosphere by first-principles calculations. *Carbon* **100**, 556–563 (2016).
18. H. I. Kim, J. R. Lince, O. L. Eryilmaz, A. Erdemir, Environmental effects on the friction of hydrogenated DLC films. *Tribol. Lett.* **21**, 51–56 (2006).
19. J. Andersson, R. A. Erck, A. Erdemir, Friction of diamond-like carbon films in different atmospheres. *Wear* **254**, 1070–1075 (2003).
20. L. Ji, H. Li, F. Zhou, W. Quan, J. Chen, H. Zhou, Effects of environmental molecular characteristics and gas–surface interaction on friction behaviour of diamond-like carbon films. *J. Phys. D Appl. Phys.* **42**, 135301 (2009).
21. A. A. Al-Azizi, O. Eryilmaz, A. Erdemir, S. H. Kim, Surface structure of hydrogenated diamond-like carbon: Origin of run-in behavior prior to superlubricious interfacial shear. *Langmuir* **31**, 1711–1721 (2015).
22. A. A. Al-Azizi, A. J. Barthel, N. D. Surdyka, J. Luo, S. H. Kim, Vapors in the ambient—A complication in tribological studies or an engineering solution of tribological problems? *Friction* **3**, 85–114 (2015).
23. O. L. Eryilmaz, A. Erdemir, Surface analytical investigation of nearly-frictionless carbon films after tests in dry and humid nitrogen. *Surf. Coat. Technol.* **201**, 7401–7407 (2007).
24. A. Erdemir, O. Eryilmaz, Achieving superlubricity in DLC films by controlling bulk, surface, and tribochemistry. *Friction* **2**, 140–155 (2014).
25. J. A. Heimberg, K. J. Wahl, I. L. Singer, A. Erdemir, Superlow friction behavior of diamond-like carbon coatings: Time and speed effects. *Appl. Phys. Lett.* **78**, 2449–2451 (2001).
26. M. J. Marino, E. Hsiao, Y. Chen, O. L. Eryilmaz, A. Erdemir, S. H. Kim, Understanding run-in behavior of diamond-like carbon friction and preventing diamond-like carbon wear in humid air. *Langmuir* **27**, 12702–12708 (2011).
27. J. Andersson, R. A. Erck, A. Erdemir, Frictional behavior of diamondlike carbon films in vacuum and under varying water vapor pressure. *Surf. Coat. Technol.* **163-164**, 535–540 (2003).
28. J. Wang, L. Shang, X. Li, Z. Lu, G. Zhang, Quantifying macroscopic friction of diamond-like carbon films by microscopic adsorption and removal of water molecules. *Langmuir* **34**, 58–65 (2018).
29. M. Tagawa, M. Ikemura, Y. Nakayama, N. Ohmae, Effect of water adsorption on microtribological properties of hydrogenated diamond-like carbon films. *Tribol. Lett.* **17**, 575–580 (2004).
30. S. J. Park, K.-R. Lee, D.-H. Ko, Tribochemical reaction of hydrogenated diamond-like carbon films: A clue to understand the environmental dependence. *Tribol. Int.* **37**, 913–921 (2004).
31. J. D. Schall, G. Gao, J. A. Harrison, Effects of adhesion and transfer film formation on the tribology of self-mated DLC contacts. *J. Phys. Chem. C* **114**, 5321–5330 (2010).
32. K. Hayashi, K. Tezuka, N. Ozawa, T. Shimazaki, K. Adachi, M. Kubo, Tribochemical reaction dynamics simulation of hydrogen on a diamond-like carbon surface based on tight-binding quantum chemical molecular dynamics. *J. Phys. Chem. C* **115**, 22981–22986 (2011).
33. T. B. Ma, L. F. Wang, Y. Z. Hu, X. Li, H. Wang, A shear localization mechanism for lubricity of amorphous carbon materials. *Sci. Rep.* **4**, 3662 (2014).
34. A. Rusanov, R. Nevshupa, J. Fontaine, J.-M. Martin, T. Le Mogne, V. Elinson, A. Lyamin, E. Roman, Probing the tribochemical degradation of hydrogenated amorphous carbon using mechanically stimulated gas emission spectroscopy. *Carbon* **81**, 788–799 (2015).
35. X. Chen, C. Zhang, T. Kato, X.-a. Yang, S. Wu, R. Wang, M. Nosaka, J. Luo, Evolution of tribo-induced interfacial nanostructures governing superlubricity in a-C:H and a-C:H:Si films. *Nat. Commun.* **8**, 1–20 (2017).
36. J. B. McClimon, A. C. Lang, Z. Milne, N. Garabedian, A. C. Moore, J. Hilbert, F. Mangolini, J. R. Lukes, D. L. Burris, M. L. Taheri, J. Fontaine, R. W. Carpick, Investigation of the mechanics, composition, and functional behavior of thick tribofilms formed from silicon- and oxygen-containing hydrogenated amorphous carbon. *Tribol. Lett.* **67**, 48 (2019).
37. C. Casiraghi, A. C. Ferrari, J. Robertson, Raman spectroscopy of hydrogenated amorphous carbons. *Phys. Rev. B* **72**, 085401 (2005).
38. J. A. Johnson, D. Holland, J. B. Woodford, A. Zinovev, I. A. Gee, O. L. Eryilmaz, A. Erdemir, Top-surface characterization of a near frictionless carbon film. *Diamond Relat. Mater.* **16**, 209–215 (2007).
39. O. L. Eryilmaz, A. Erdemir, TOF-SIMS and XPS characterization of diamond-like carbon films after tests in inert and oxidizing environments. *Wear* **265**, 244–254 (2008).
40. T. Kuwahara, G. Moras, M. Moseler, Friction regimes of water-lubricated diamond (111): Role of interfacial ether groups and tribo-induced aromatic surface reconstructions. *Phys. Rev. Lett.* **119**, 096101 (2017).
41. A. P. Hitchcock, D. C. Newbury, I. Ishii, J. Stöhr, J. A. Horsley, R. D. Redwing, A. L. Johnson, F. Sette, Carbon K-shell excitation of gaseous and condensed cyclic hydrocarbons: C_3H_6, C_4H_8, C_5H_8, C_5H_{10}, C_6H_{10}, C_6H_{12}, and C_8H_8. *J. Chem. Phys.* **85**, 4849–4862 (1986).
42. J. Pawela-Crew, R. J. Madix, J. Stöhr, The effect of subsurface oxygen on the orientation of molecular oxygen on Ag(110). *Surf. Sci.* **339**, 23–28 (1995).
43. J. L. Solomon, R. J. Madix, J. Stöhr, Orientation and absolute coverage of benzene, aniline, and phenol on Ag(110) determined by NEXAFS and XPS. *Surf. Sci.* **255**, 12–30 (1991).
44. J. L. Solomon, R. J. Madix, W. Wurth, J. Stöhr, NEXAFS and EELS study of the orientation of sulfur dioxide on silver(110). *J. Phys. Chem.* **95**, 3687–3691 (1991).
45. D. D'Angelo, C. Bongiorno, M. Amato, I. Deretzis, A. La Magna, E. Fazio, S. Scalese, Oxygen functionalities evolution in thermally treated graphene oxide featured by EELS and DFT calculations. *J. Phys. Chem. C* **121**, 5408–5414 (2017).
46. O. Lichtenberger, D. Neumann, A study of Si-L and O-K ELNES in plant material: SiO_2, Ca- and Zn-silicate in *Minuartia*. *J. Microsc.-Oxford* **183**, 45–52 (2003).
47. G. Moras, L. Pastewka, P. Gumbsch, M. Moseler, Formation and oxidation of linear carbon chains and their role in the wear of carbon materials. *Tribol. Lett.* **44**, 355–365 (2011).
48. G. Moras, L. Pastewka, M. Walter, J. Schnagl, P. Gumbsch, M. Moseler, Progressive shortening of sp-hybridized carbon chains through oxygen-induced cleavage. *J. Phys. Chem. C* **115**, 24653–24661 (2011).
49. F. G. Sen, Y. Qi, A. T. Alpas, Material transfer mechanisms between aluminum and fluorinated carbon interfaces. *Acta Mater.* **59**, 2601–2614 (2011).
50. Y. Morita, S. Jinno, M. Murakami, N. Hatakeyama, A. Miyamoto, A computational chemistry approach for friction reduction of automotive engines. *Inl. J. Engine Res.* **15**, 399–405 (2014).
51. T. Onodera, K. Kawasaki, T. Nakakawaji, Y. Higuchi, N. Ozawa, K. Kurihara, M. Kubo, Effect of tribochemical reaction on transfer-film formation by poly(tetrafluoroethylene). *J. Phys. Chem. C* **118**, 11820–11826 (2014).
52. X. Chen, T. Kato, M. Kawaguchi, M. Nosaka, J. Choi, Structural and environmental dependence of superlow friction in ion vapour-deposited a-C:H:Si films for solid lubrication application. *J. Phys. D Appl. Phys.* **46**, 255304 (2013).
53. H. Bhaskaran, B. Gotsmann, A. Sebastian, U. Drechsler, M. A. Lantz, M. Despont, P. Jaroenapibal, R. W. Carpick, Y. Chen, K. Sridharan, Ultralow nanoscale wear through atom-by-atom attrition in silicon-containing diamond-like carbon. *Nat. Nanotechnol.* **5**, 181–185 (2010).
54. A. Verdaguer, G. M. Sacha, H. Bluhm, M. Salmeron, Molecular structure of water at Interfaces: Wetting at the nanometer scale. *Chem. Rev.* **106**, 1478–1510 (2006).
55. D. B. Asay, A. L. Barnette, S. H. Kim, Effects of surface chemistry on structure and thermodynamics of water layers at solid vapor interfaces. *J. Phys. Chem. C* **113**, 2128–2133 (2009).
56. D. B. Asay, S. H. Kim, Evolution of the adsorbed water layer structure on silicon oxide at room temperature. *J. Phys. Chem. B* **109**, 16760–16763 (2005).
57. H. Washizu, S. Sanda, S.-a. Hyodo, T. Ohmori, N. Nishino, A. Suzuki, Molecular dynamics simulations of elasto-hydrodynamic lubrication and boundary lubrication for automotive tribology. *J. Phys. Conf. Ser.* **89**, 012009 (2007).
58. W. H. Briscoe, S. Titmuss, F. Tiberg, R. K. Thomas, D. J. McGillivray, J. Klein, Boundary lubrication under water. *Nature* **444**, 191–194 (2006).
59. R.-G. Xu, Y. Leng, Squeezing and stick-slip friction behaviors of lubricants in boundary lubrication. *Proc. Natl. Acad. Sci. U.S.A.* **115**, 6560–6565 (2018).
60. T. Kuwahara, G. Moras, M. Moseler, Role of oxygen functional groups in the friction of water-lubricated low-index diamond surfaces. *Phys. Rev. Mater.* **2**, 073606 (2018).
61. X. Chen, T. Kato, Growth mechanism and composition of ultrasmooth a-C:H:Si films grown from energetic ions for superlubricity. *J. Appl. Phys.* **115**, 044908 (2014).

Acknowledgments: We acknowledge T. Kato and M. Nosaka for the assistance in deposition of amorphous carbon films. **Funding:** This research is funded by the National Natural Science Foundation of China (grant nos. 51605247, 51975314, 51527901, and 51727901). **Author contributions:** X.C., C.Z., and J.L. designed research. X.C., X.Y., W.Q., J.C., S.W., and R.W. performed research. X.C., X.Y., S.W., and R.W. analyzed data. X.C., X.Y., and C.Z. wrote the paper. All authors commented on the manuscript. **Competing interests:** The authors declare that they have no competing interests. **Data and materials availability:** All data needed to evaluate the conclusions in the paper are present in the paper and/or the Supplementary Materials. Additional data related to this paper may be requested from the authors.

Submitted 10 July 2019
Accepted 2 January 2020
Published 27 March 2020
10.1126/sciadv.aay1272

Citation: X. Chen, X. Yin, W. Qi, C. Zhang, J. Choi, S. Wu, R. Wang, J. Luo, Atomic-scale insights into the interfacial instability of superlubricity in hydrogenated amorphous carbon films. *Sci. Adv.* **6**, eaay1272 (2020).